ORIGINAL PAPER

Effect of 3D grain structure representation in polycrystal simulations

Devin M. Pyle · Jing Lu · David J. Littlewood · Antoinette M. Maniatty

Abstract Simulation results from finite element models using two types of 3D polycrystal geometric representations, one with a voxel representation and stair-stepped grain boundaries and the other with smooth grain boundaries, are compared. Both models start with a periodic grain structure representation, which is in the form of a regular, rectangular 3D array of points, where each point is assigned an orientation. The voxel representation is obtained by simply sampling the array of grid points on a coarser regular grid with a prescribed resolution and forming a voxel centered at each grid point, which is assigned the grain orientation from the sampled grid point. The voxel representation may be meshed directly by decomposing each voxel into finite elements. In the second case, a method is presented that extracts geometric topology information for a grain structure with smooth, flat grain boundaries from the discrete grain structure representation. From the geometric topology information, a finite element mesh is created. The two representations are then subjected to large strain deformations, and the simulation results and efficiencies are compared. The macroscopic behavior, overall texture evolution, and statistical distribution of stress and slip are found to be nearly identical for both models. However, noticeable differences are observed in the misorientation distribution within grains and the smoothness of the stress field. The voxel representation is found to be more efficient because of the uniform finite element mesh.

Keywords Crystal plasticity · Finite element method · Polycrystal · Topology

D. M. Pyle · J. Lu · D. J. Littlewood · A. M. Maniatty (✉)
Department of Mechanical, Aerospace, and Nuclear Engineering,
Rensselaer Polytechnic Institute, Troy, NY 12180-3590, USA
e-mail: maniaa@rpi.edu

D. M. Pyle
e-mail: pyled@rpi.edu

J. Lu
e-mail: Jing.Lu@sbmoffshore.com

Present Address:
J. Lu
SBM Atlantia, Houston, TX, USA

D. J. Littlewood
e-mail: djlittl@sandia.gov

Present Address:
D. J. Littlewood
Sandia National Laboratories, Albuquerque, NM, USA

1 Introduction

The macroscopic, mechanical behavior of polycrystalline metals is dictated by underlying smaller scale phenomena occurring over a range of scales. One of the most informative scales, in this multiscale perspective, is the grain scale. At the grain scale, important characteristics of the microstructure, such as grain size, shape and orientation distribution, are evident. These characteristics are strongly related to the macroscale behavior, both during processing of the metal and in-service. For example, the initial microstructure, before thermal-mechanical processing, has a strong impact on the final microstructure and also influences the deformation behavior. In-service, the grain structure characteristics affect the anisotropy, strength, and ductility. It should also be mentioned that the grain scale is not the only important scale, and that for a grain scale constitutive model to be accurate, it should be based on smaller scale phenomena, in particular, dislocation phenomena.

Because of the importance of the grain scale in developing predictive models of the behavior of metallic materials, numerous researchers have developed approaches for

modeling polycrystals. That work can be divided into two categories: (a) models that assume a homogeneous deformation and stress within each grain and take the macroscopic deformation and stress to be the average over all the grains, which allow the grains to be modeled without an explicit representation, and (b) models that explicitly represent the grain structure in order to capture the heterogeneous deformation and stress fields that occur within grains due to interactions with neighboring grains. Examples of the first category include: the Taylor model [1–3], where each grain is assumed to undergo the macroscopic deformation; the relaxed constraint model for distorted, elongated grains [4, 5], where the macroscopic deformation is prescribed along some directions and the macroscopic stress is prescribed along other directions in the flat part of the grains; and self-consistent approaches [6], where each grain is treated as embedded in a homogeneous equivalent medium. While these approaches provide useful predictions regarding texture evolution and macroscopic stress–strain response, they do not capture the intra-grain heterogeneities, which are important contributors to certain physical processes and considered in the second category of polycrystal models. For example, grain size effects are attributed to gradients in deformation fields that arise in grains due to interactions with neighboring grains, see for example Fleck and Hutchinson [7], Beaudoin et al. [8], and Janssen et al. [9]. The formation of nucleation sites for recrystallization results from portions of a single grain rotating into different orientations due to constraints imposed by surrounding grains leading to low angle grain boundaries, see for example Beaudoin et al. [10] and Sarma et al. [11]. Fatigue crack initiation may occur at grain boundaries or constituent particles and is related to the local grain orientations [12]. For a more comprehensive review of crystal plasticity modeling, Roters et al. [13] provides an excellent overview of constitutive models and multiscale methods for modeling crystalline materials.

In order to capture the heterogeneous fields arising within the grains of a polycrystal, many researchers explicitly model the grain structure, most commonly using finite element discretizations of polycrystals. Of the explicit polycrystal models, a number of different geometric representations of the polycrystals have been considered. The simplest approach uses uniform brick elements, where each brick may constitute a single grain [14, 15], or where groups of brick elements are defined as grains [11, 16–18]. The former case is not sufficiently refined to capture local variations that occur within grains. The latter case results in stair-stepped grain boundaries if irregular grain shapes are modeled. The natural question that arises with regard to the latter approach is whether such a topological representation, where the grain boundaries are stair-stepped, might lead to inaccurate results, especially near the grain boundaries, which may be a region of key importance. A regular mesh may also be used to model irregular grain structures, where the orientations are defined at the integration points instead of the grain boundaries, which eliminates the stair-stepped nature but does not create smooth grain boundaries [19]. An alternate approach that allows for multiple finite elements within a grain to capture intragranular field variations without stair-stepped boundaries is to model regular arrays of uniformly shaped grains. In Beaudoin et al. [8], groups of brick elements in a uniform grid are distorted to form Wigner–Seitz cells. Ritz and Dawson [20] compare the stress distributions resulting from four different regular grain representations, where groups of tetrahedral elements were used to form grains of cubic, rhombic, dodecahedral, and truncated octahedral shapes. In that work, similar trends were observed in the stress distributions across the geometric representations, but with differences in the level of intra- and inter-granular variability because of differences in levels of geometric constraint. These methods provide a smooth, more accurate representation, but the grains are still uniform and regular, and thus, the natural variability of the grain structure is not captured. In recent years, researchers have used Voronoi tesselations to define the grain structure and then meshed with tetrahedral elements [21–24]. However, the grain representations produced by straight Voronoi tesselations are not as accurate as those defined using methods described in the next paragraph, which generate typically a regular, rectangular grid of points, where each point is assigned an orientation.

There are many methods to generate grain structures based on the approach of simulating the phenomenon of grain growth. The popular ones are the Monte Carlo (Potts) [25, 26], phase field [27], and cellular automaton [28] methods. Each of these methods treat microstructures as thermodynamically unstable, and evolve the microstructure with the goal of minimizing total free energy. The microstructure representations that result from these models are typically a regular grid of points in 3D space, with each point assigned an orientation, and where groups of neighboring points with the same orientation constitute a grain. An alternative approach to these methods, which is not based on grain growth, but rather seeks to directly represent the grain structure, also as a regular grid of points in 3D space, with a statistically similar representation is described by Saylor et al. [29]. A similar approach is used in St-Pierre et al. [30], where the representative volume is filled with non-overlapping ellipsoids with the size and aspect ratio distributions found from experimental observations, and then the space is filled by grid points, where each grid point is assigned to a grain based on what ellipsoid it lies in or is closest to. Finally, it should also be mentioned that 3D grain structure representations of actual grain structures may be obtained experimentally using electron backscatter diffraction (EBSD) to image a series of 2D slices, where a focused ion beam (FIB) is used to remove material between successive 2D slices [23, 24, 31] or through

3D X-Ray diffraction [32]. This also typically generates a 3D regular grid representation of the grain structure.

The present work compares the results of explicit polycrystal simulations for two different topological representations, one with a voxel representation with stair-stepped grain boundaries, which we will refer to as voxel topology (VT) and one where the polycrystals have smooth, flat grain boundaries, which we will refer to as smooth topology (ST). A similar comparison was presented in Kanit et al. [21] for a two-phase, linear, elastic material, where each phase was isotropic, and they found that in small models the average results for stress and strain matched, and field fluctuations differed slightly. In this work, we consider large strains in anisotropic, elasto-viscoplastic polycrystals. We also present a procedure for creating the smooth grain boundary representation from the regular grid data that allows for finite element meshing. For both implementations, we start with a modified Monte Carlo (Potts) model, based on that presented in Radhakrishnan and Zacharia [26], for generating the simulated grain structure represented by a regular array of grid points, where each point is assigned an orientation. Here, the model is modified to generate a periodic microstructure. Currently, this work is limited to relatively equi-axed grains of a single phase material, which this procedure generates. Next, we apply a procedure for removing small features based on prescribed criteria. The VT model can be created directly by sampling the grid points on a grid of the same or coarser resolution, creating a voxel centered at each sampled grid point, and sub-dividing each voxel into finite elements. After this, we present an approach for extracting topology information, specifically vertices, edges, patches, and regions, which is used to define the ST geometric model of the grain structure. A standard 3D finite element mesher can be used given the topology information. The VT and ST models are generated so that the number of elements in the resulting finite element meshes for each topological representation are comparable allowing for direct local comparisons to be made. Both models are then deformed to a large strain (20 % plane strain compression), and the resulting orientation, misorientation, stress, and slip fields are compared between the models, and conclusions are drawn. The relative computational efficiency of each model is also compared.

2 Generating polycrystal models

In order to compare the results of simulations with voxel and smooth topologies, it is first necessary to define comparable models. A data set of orientations assigned to a regular array of grid points representing a polycrystal is required first. Here, a modified Monte Carlo approach, described next, is used to define the initial data set defining the model polycrystal, however, any approach that creates a regular grid

array polycrystal representation may be used as a starting point. After that, the VT and ST representations and associated finite element meshes are created. The approach for each is described below.

2.1 Modified Monte Carlo simulation

The first step in generating the polycrystal representations involves creating a 3D polycrystal unit cell using a modified Monte Carlo grain growth algorithm based on that presented in Radhakrishnan and Zacharia [26], which is summarized here. First, a 3D structured grid point domain of $N \times N \times N$ is chosen, with each grid point in the domain given a unique orientation number. Then, in each step of the simulation, one grid point is chosen randomly, and its orientation switched to that of a nearest neighbor randomly selected. The energy change of the local cluster associated with this switching is then calculated. If the local cluster energy is lowered, the new orientation is kept; otherwise, the orientation is switched back to its previous value. The local cluster energy is calculated using

$$E = -J \left[\sum_{j=1}^{n} \delta_{s_0 s_j} \right] \tag{1}$$

where J is a constant being proportional to the grain boundary energy, δ_{ij} is the Kronecker δ function, S_0 is the orientation number of the grid point whose orientation change is being attempted, S_j is the orientation number of a nearest neighbor, and n is the number of nearest neighbors, 26 in our case. The goal of the microstructure evolution is to reduce grain boundary energy. Intuitively, we can imagine that the generated grain structures will be of convex shape with flat facets and straight edges since that is the most efficient way of constructing grains. Furthermore, since this energy function is isotropic, the grains will be on average equi-axed.

The evolution is counted by the Monte Carlo Steps (MCS), where each Monte Carlo Step is $N \times N \times N$ orientation switching attempts. The grain growth continues until the number of remaining grains reaches a specific value. In order to link to the macro-scale, these polycrystals are designed to have periodic boundaries by assuming opposite faces of the polycrystal are linked and neighboring each other. In this work, a generated microstructure with 107 grains and 180 regions, comprised of $200 \times 200 \times 200$ grid points is created. There are more geometric regions than grains due to periodicity, i.e., the grains wrap around to the opposite side of the geometric model splitting the grain into multiple regions.

2.2 Small feature elimination

Before extracting the two topological representations considered here, for simulation efficiency, small features in the
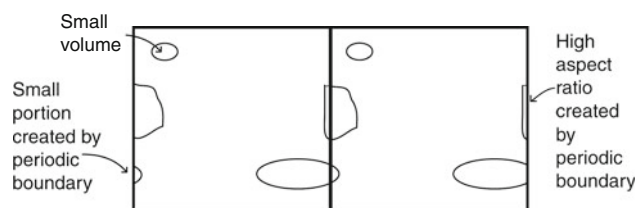
Fig. 1 2D sketch showing three types of small features

model should be eliminated or reduced as much as possible. The small features may include small grains generated by the Monte Carlo grain growth simulation (if the modeler decides these are not important), and small volume and high aspect ratio portions generated by periodic unit cell boundaries cutting through grains on the boundary (Fig. 1). The positions of the periodic unit cell boundaries are adjusted so that the least number of small features are created. Since the polycrystal example described here is made up of $200 \times 200 \times 200$ grid points, there are 200 possible locations for the periodic boundaries in each of the three dimensions. All 200 possible positions are tested in each dimension and the optimal positions chosen.

2.3 Geometric model representations

Two different geometric representations of the polycrystal model are considered and meshed for finite element simulation. The VT and ST models are meshed with similar numbers of quadratic, tetrahedral elements for comparison, and three meshes are created for each model in order to test for mesh convergence as well as to investigate simulation efficiency. The meshes are designed to have roughly 1,000; 1,300 and 1,800 elements per grain. First, the simpler voxel topology model is described briefly, and then a method is presented to generate the smooth topology model.

2.3.1 Voxel topology model

The voxel topology (VT) model is relatively straightforward to create and mesh once the discrete model is generated. In this work, in order to create finite element models with a comparable number of elements to compare to the smooth models, we sample the grid points generated from the Monte Carlo procedure, with 200 grid points along each direction, onto coarser grids to define the VT model. In order to obtain the desired number of elements per grain, as mentioned above, we choose three grid sizes, with 26, 29, and 32 grid points along each direction. The center of each sampled grid point is taken as a voxel center, and the voxel boundaries are centered between sampled grid points. Each voxel is assigned the grain orientation identity of the grid point at its center. Meshing this topology involves simply meshing each

voxel. Here, each voxel is divided into 6 congruent, quadratic, tetrahedral finite elements, resulting in meshes with 105,456 elements, 146,334 elements, and 196,608 elements. This method also naturally aligns the nodal points on opposing faces allowing for these nodes to be constrained if periodic boundary conditions are used. The three VT models created are shown in Fig. 2.

2.3.2 Smooth topology model

A procedure for extracting a smooth topological representation from the discrete 3D regular, rectangular grid representation was developed and used in this work. The approach taken here is based on the well-known Marching Cubes algorithm [33] used widely in the field of visualization. Constructing geometric topology from 3D scalar fields is sometimes referred to as "3D surface reconstruction" or "polygonizing 3D scalar fields" [34]. In visualization applications, it is not critical to avoid overlap or penetration, which may occur with the Marching Cubes algorithm, but overlap or penetration is a problem for constructing a finite element model. Numerous methods have been developed to overcome this problem, including the modified Marching Cubes [35], Marching Tetra-cubes [36] and Marching Intersections [37] methods. In Wiederkehr et al. [38], the modified Marching Cubes method is used, following the procedure developed in [35,39] to generate a consistent topology of a microstructural representation, which is subsequently meshed for finite element analysis. Here, a fairly simple approach is devised that focuses on the voxels lying at the grain boundaries. The first step is to sift out the boundary cubes, where each cube is defined by eight grid points that make up the corners of the cube, each with an assigned orientation from the Monte Carlo procedure. Boundary cubes are the cubes that lie on the boundary between grains, having grid points of different orientation values. It is these boundary cubes that collectively represent the interfaces between different grains, and provide the basis for geometric model construction. There are two important properties associated to each boundary cube: the x, y, and z coordinates of the weighted center of the eight grid points of this cube (that will be used as the location of the geometric entity), and the orientations of the grid points at the corners of the cube (which provides connections between boundary cubes). The weighted center of a boundary cube is found by partitioning the eight grid points of the cube by their orientations, finding the center of each group with a common orientation, defining the weight for each group as the fraction of the eight grid points that has that common orientation, and then adding the center of each group multiplied by its weight.

The boundary cubes are organized into geometric entities (vertices, edges, patches, regions) by considering the number of different orientations associated with the grid points defining each boundary cube. Interfaces (grain boundaries) are
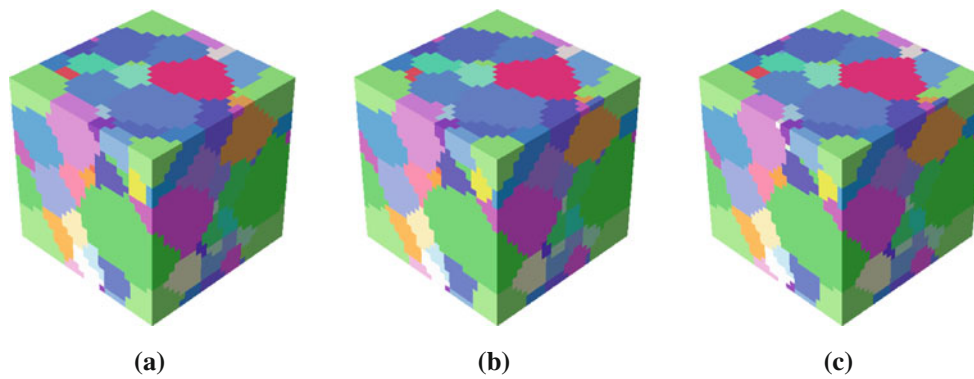
Fig. 2 Three VT model representations with **a** 26 voxels, **b** 29 voxels, and **c** 32 voxels, along each edge

at locations where two regions (i.e., two grain orientations) meet, edges at locations where three regions meet, and vertices at locations where four or more regions meet. Since the polycrystal models are generated with the goal of reducing interfacial regions, the above simple rules are well followed. Technically, it is possible to have an edge where four regions meet, but those cases are energetically unfavorable (in the sense of creating unnecessary grain boundary regions), and rarely occur. In fact, such a case has not been observed in our models and is typically not seen in real microstructures of single phase materials, where grains are normally observed to meet at triple points in 2D sections (which corresponds to three grains meeting to form an edge) and not at quadruple points (which would correspond to four grains meeting at an edge), see, for example, Cahn [40].

First, the vertices are identified followed by the edges that connect them. The weighted center point of these vertex cubes is regarded as the vertex location. Edge cubes containing the same three orientations are on the edge where grains with those three orientations meet. Since these three orientations are also associated with the vertices on the two ends of the edge, the two end vertices can be found and an edge is created by connecting these two vertices (Fig. 3). To test the accuracy of using this straight line to represent the real edge made up of edge cubes, the distance from each of the edge cubes associated with this edge to the created edge is calculated and the maximum distance is defined as the "error" of this edge (Fig. 4). Here, we choose 1.0 (the distance between neighboring grid points) as the critical "error" value, where a typical edge is made up of more than ten edge cubes. If the error of an edge is smaller than 1.0, we regard it as straight and keep the edge created by connecting the two vertices, otherwise, we split the edge into two straight edges by inserting a new vertex at the location of the edge cube having the maximum error. Typically, only about 10 % of the edges created have an "error" larger than 1.0, meaning that most of the edges are straight, and that the previous assumption (that all interfaces are of 3D polygon shape) is valid. The
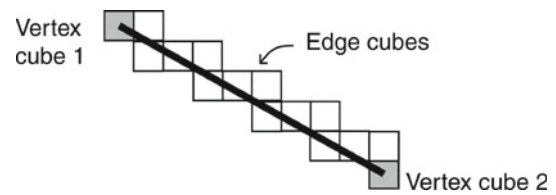

Fig. 3 2D sketch showing edge creation based on corresponding edge cubes and vertex cubes. *Shaded cubes* are vertex cubes, others are edge cubes
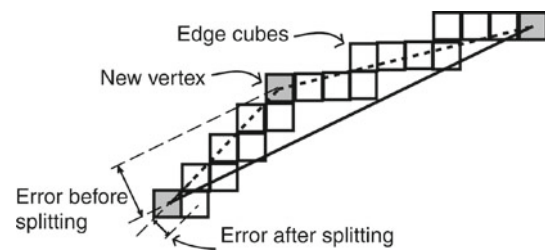

Fig. 4 2D sketch showing edge-split operation used to increase the accuracy of the constructed edge. *Shaded cubes* are vertex cubes, other cubes are edge cubes

splitting procedure was only applied once to avoid creating short edges.

Similarly, interface cubes with the same two orientation values collectively form an interface, and the two orientation values are also associated with the edges enclosing the interface. Edges associated with this interface are found in order to form an edge loop. If all the edges are lying on the same plane, this interface is a patch; otherwise this interface is triangulated by either introducing a vertex around the center of the interface, or just connecting the existing vertices (Fig. 5). All possible splitting choices are tested, and the one which maximizes the minimum angle of all the angles of the triangulation is used. It should be noted that this procedure assumes flat interfaces, taking advantage of the fact that flat interfaces are energetically favorable. If the interfaces between the grains are not flat, error is introduced.
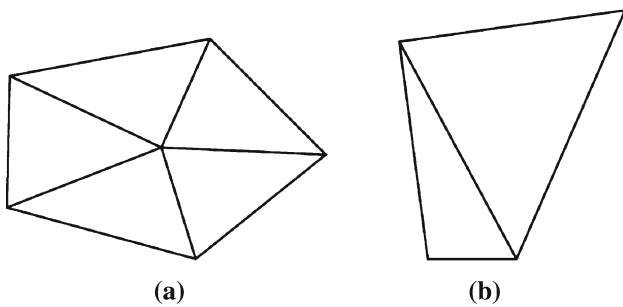
Fig. 5 Two ways of triangulation: **a** by introducing a new vertex; **b** by connecting existing vertices

After all patches are constructed, the region-patch connection is established by tracing the common orientation values between regions and patches. The complete geometric structure is constructed and no further polishing is needed.

A 3D mesh is then generated using Abaqus FEA software [41]. Because of the periodicity of the grain structure, while there are twelve edges on the polycrystal model, there are only three unique edge discretizations. For example, all of the edges parallel to the x axis cut through the same grains and have the same discretization. Thus, each of the three independent edges is meshed first with 1D meshes that are then copied to remaining edges. Next, three sides sharing one corner of the unit cell are each given a surface mesh, where the mesh is seeded by the discretization already done on the edges. The surface mesh is then copied to the three remaining opposite sides so that periodic boundary conditions may be easily applied by constraining matching nodes on opposite faces. Finally the interior volume is fully meshed, insuring periodicity. Three meshes were created with varying levels of refinement: 104,165; 146,918; and 194,297 elements. Figure 6 shows the resulting meshed grain structure, comparing the meshed VT model described in the preceding Sect. (2.3.1) and the ST model described here with the finest meshes used in this work, that is with 196,608 and 194,297 elements, respectively.

3 Material model

The grain-scale constitutive model used in the finite element implementation is presented in this section. In this work, aluminum alloy 7075-T651 is modeled, which is a face-centered cubic (fcc) metal with twelve primary $\{111\}\langle110\rangle$ slip systems. The derivation of the constitutive model along with the calibration of material parameters is given in [42], and a summary is presented here. The tensor notation used herein follows that in Gurtin [43]. First, a multiplicative decomposition of the deformation gradient into its elastic and plastic parts [44] is assumed

$$F = F^e F^p \tag{2}$$

where F^p is the plastic deformation gradient and F^e is the elastic deformation gradient. The Green-Lagrange elastic strain tensor is then $\hat{E}^e = \frac{1}{2}(F^{eT} F^e - I)$.

A hyperelastic potential is used for the elastic response. Specifically, the following simple quadratic form is used

$$\hat{W}(\hat{E}^e) = \frac{1}{2} \hat{E}^e \cdot \hat{\mathcal{L}}[\hat{E}^e] \tag{3}$$

where $\hat{\mathcal{L}}$ is the fourth order elasticity tensor, which is defined in terms of the three independent elasticity parameters for crystals with cubic symmetry, C_{11}, C_{12}, and C_{44}, and the $\hat{}$ indicates the relaxed, elastically unloaded configuration. The second Piola-Kirchoff stress, $\hat{S}$ is then

$$\hat{S} = \frac{\partial \hat{W}}{\partial \hat{E}^e} = \hat{\mathcal{L}}[\hat{E}^e] \tag{4}$$

and the Cauchy stress, σ, on the deformed configuration is

$$\sigma = \frac{1}{det(F^e)} F^e \hat{S} F^{eT} \quad . \tag{5}$$

For the viscoplastic response, the rate of shearing, $\dot{\gamma}^\alpha$, is taken to be related to the resolved shear stress, τ^α, on the α slip system through a power law

$$\dot{\gamma}^\alpha = \dot{\gamma}_0 \frac{\tau^\alpha}{g^\alpha} \left| \frac{\tau^\alpha}{g^\alpha} \right|^{1/m - 1} \tag{6}$$

where $\dot{\gamma}_0$ is the reference shearing rate, m is the strain rate sensitivity, and g^α is the slip resistance. The resolved shear stress on a slip system is related to the second Piola-Kirchhoff stress through

$$\tau^\alpha = \left(F^{eT} F^e \hat{S} \right) \cdot \hat{P}^\alpha, \quad \hat{P}^\alpha = \left(\hat{s}^\alpha \otimes \hat{m}^\alpha \right) \tag{7}$$

where $\hat{P}^\alpha$ is the Schmid tensor defined in terms of the slip direction and slip plane normal, $\hat{s}^\alpha$ and $\hat{m}^\alpha$, respectively, for slip system α. The relationship between the plastic deformation gradient and the rate of shearing on the slip systems is

$$\hat{L}^p = \dot{F}^p (F^p)^{-1} = \sum_{\alpha=1}^{N_s} \dot{\gamma}^\alpha \hat{P}^\alpha \tag{8}$$

where $\hat{L}^p$ is the plastic velocity gradient. The resistance to plastic slip, g^α, which describes the hardening behavior, evolves according to

$$\dot{g}^\alpha = G_0 \left(\frac{g_s - g^\alpha}{g_s - g_o} \right) \sum_{\beta=1}^{N_s} H^{\alpha\beta} |\dot{\gamma}^\beta| \tag{9}$$

where g_0 is the initial slip resistance on all the slip systems, G_0 is the hardening rate coefficient, g_s is the saturation hardness, and $H^{\alpha\beta}$ is the slip interaction matrix which describes the relative strength of latent and self hardening on the slip
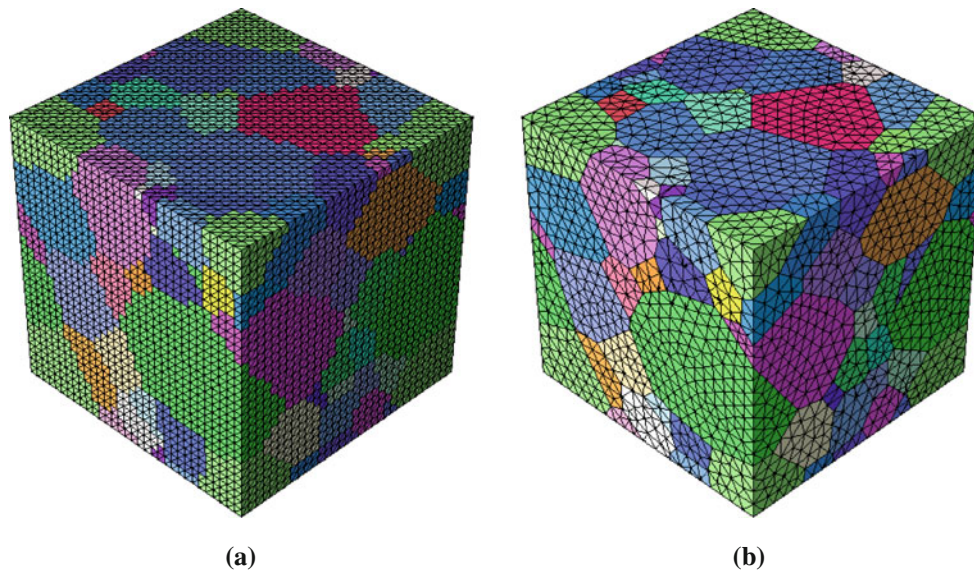
Fig. 6 Meshed 107 grain structure: **a** voxel topology and **b** smooth topology

systems. In this work, we model aluminum alloy 7075-T651, which is a dispersion strengthened alloy, where hardening is associated with dislocations bowing out and forming loops around precipitates. Hardening is caused by incompatibilities between the plastic strain field due to slip and the elastic precipitates. The resulting form of the hardening matrix is

$$H^{\alpha\beta} = \left| \hat{\boldsymbol{M}}^{\alpha} \cdot \hat{\mathcal{L}} \left[\left(\hat{\boldsymbol{\mathcal{Y}}} - \mathcal{I} \right) [\hat{\boldsymbol{M}}^{\beta}] \right] \right| \tag{10}$$

where $\hat{\boldsymbol{M}}^{\alpha}$ is the symmetric part of the Schmid tensor, $\hat{\boldsymbol{P}}^{\alpha}$, $\hat{\boldsymbol{\mathcal{Y}}}$ is the average Eshelby tensor associated with the precipitates (approximated as elliptical), and $\mathcal{I}$ is the fourth order identity tensor. For details of the model derivation and calibration of material parameters, see Bozek et al. [42]. The model parameters for AA7075-T651 are given here in Tables 1 and 2 for completeness.

4 Finite element implementation

The model is implemented in parallel into a 3D finite element framework using an integration algorithm described in [45] and a finite element formulation with a consistent tangent similar to that described in [46]. A mixed displacement/pressure finite element formulation is used with P2/P1 tetrahedral elements, specifically quadratic displacement interpolation and linear, discontinuous pressure interpolation. The pressure is eliminated at the element level so that the nonlinear finite element procedure only solves for the displacement degrees of freedom. Periodic boundary conditions are implemented where the formulation is defined in terms of the displacement fluctuation field with the fluctuations constrained to match on opposite faces [47], effectively treating the modeled unit cell as replicated on each side. For information regarding specific details of the integration algorithm, finite element implementation, or derivation of the consistant tangent, see [48]. The open source software toolkit PETSc is used for parallel solution of the resulting equations using the conjugate gradient method with a block Jacobi pre-conditioner [49].

5 Simulation results

In order to compare the VT and ST representations, we model plane strain compression to a 20 % reduction over 20 seconds in the 107 grain structure. The deformation is defined such that the material is compressed along ND, lengthened along RD, and TD is the zero strain direction, as typical for rolling. The grain structure was assigned a set of random orientations. The VT and ST models are shown in Fig. 7 without meshes, where the colors indicate the grain orientations using the inverse pole figure color map shown.

5.1 Mesh convergence and efficiency

As mentioned before, the VT and ST models were meshed with similar numbers of quadratic, tetrahedral elements for comparison, and three meshes were created for each model in order to test mesh convergence as well as to investigate simulation efficiency. Table 3 lists the number of elements and degrees of freedom for each model.
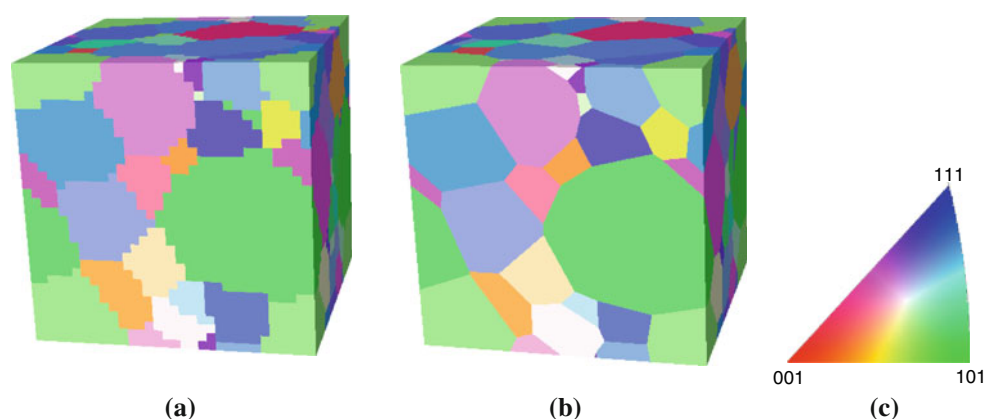
For checking mesh convergence, we only look at the difference in results between the different meshes for each

Table 1 Material parameters for AA7075-T651

m	$\dot{\gamma}_0$ (s^{-1})	g_0 (MPa)	G_0 (MPa)	g_s (MPa)	C_{11} (GPa)	C_{12} (GPa)	C_{44} (GPa)
0.005	1.0	220	120	250	107.3	60.9	28.3

Table 2 Hardening interaction matrix ($H^{\alpha\beta}$) and slip system numbering

Slip	System	ID	1	2	3	4	5	6	7	8	9	10	11	12
(111)	[1$\bar{1}$0]	1	1.0	0.50	0.50	0.50	0.59	0.088	0.088	0.50	0.59	0.18	0.088	0.088
(111)	[$\bar{1}$01]	2	0.50	1.0	0.50	0.59	0.50	0.088	0.18	0.088	0.088	0.088	0.59	0.50
(111)	[01$\bar{1}$]	3	0.50	0.50	1.0	0.088	0.088	0.18	0.088	0.59	0.50	0.088	0.50	0.59
($\bar{1}$11)	[101]	4	0.50	0.59	0.088	1.0	0.50	0.50	0.59	0.50	0.088	0.088	0.18	0.088
($\bar{1}$11)	[1$\bar{1}$0]	5	0.59	0.50	0.088	0.50	1.0	0.50	0.088	0.088	0.18	0.59	0.088	0.50
($\bar{1}$11)	[01$\bar{1}$]	6	0.088	0.088	0.18	0.50	0.50	1.0	0.50	0.59	0.088	0.50	0.088	0.59
(1$\bar{1}$1)	[$\bar{1}$01]	7	0.088	0.18	0.088	0.59	0.088	0.50	1.0	0.50	0.50	0.50	0.59	0.088
(1$\bar{1}$1)	[0$\bar{1}$$\bar{1}$]	8	0.50	0.088	0.59	0.50	0.088	0.59	0.50	1.0	0.50	0.088	0.088	0.18
(1$\bar{1}$1)	[110]	9	0.59	0.088	0.50	0.088	0.18	0.088	0.50	0.50	1.0	0.59	0.50	0.088
($\bar{1}$$\bar{1}$1)	[$\bar{1}$10]	10	0.18	0.088	0.088	0.088	0.59	0.50	0.50	0.088	0.59	1.0	0.50	0.50
($\bar{1}$$\bar{1}$1)	[101]	11	0.088	0.59	0.50	0.18	0.088	0.088	0.59	0.088	0.50	0.50	1.0	0.50
($\bar{1}$$\bar{1}$1)	[0$\bar{1}$$\bar{1}$]	12	0.088	0.50	0.59	0.088	0.50	0.59	0.088	0.18	0.088	0.50	0.50	1.0

Fig. 7 107 grain models used in the simulations for comparison where the grain orientations are depicted with an inverse pole figure color map with respect to the ND sample direction: **a** VT model, **b** ST model, and **c** inverse pole figure color map legend

model representation type (VT and ST), and in the next section we will compare the VT and ST results with each other in more detail. First, we consider the difference in the grain sizes between the different representations. The ST models all have exactly the same grain sizes because they are based on the same geometric model. The differences in grain sizes between the VT and ST models relative to the average grain size are 1.58, 1.34, and 0.97 % on average, for the coarsest to finest VT models, with maximum differences of 6.89, 6.24, and 4.30 %.

The variability in the stress is an important quantity that we study here, and so we will first look at the average and standard deviation in the stress for the different meshes. The resulting volume average and standard deviation in the von

Mises effective stress for each mesh is given in Table 3 at 15 and 20 % compression. The von Mises effective stress is first computed in each element and then the volume average and standard deviation in the von Mises stress are evaluated for the polycrystal. The results for individual stress components are similar, with the difference in average and standard deviation in the stress between the finest and the intermediate mesh less than 1.5 and 2.2 MPa, respectively, and between the finest and coarsest mesh less than 2.5 and 3 MPa, respectively, for any stress component. It should be noted that no values are given in Table 3 for 20 % compression for the coarsest ST mesh because the simulation failed at 18 % compression due to element distortion, which is explained in more detail below.

Table 3 Mesh convergence study data at 15 and 20 % compression (*dof* number of degrees of freedom)

No. elements	dof	15 %		20 %	
		$\bar{\sigma}$ (MPa)	Σ_σ (MPa)	$\bar{\sigma}$ (MPa)	Σ_σ (MPa)
Voxel					
105,456	446,631	670.5	101.2	683.4	103.1
146,334	616,137	669.3	100.7	682.7	102.3
196,608	823,875	668.3	100.5	681.5	102.4
Smooth					
104,165	434,274	666.3	99.0		
146,918	605,187	665.0	98.7	677.3	100.6
194,297	794,664	664.4	98.3	677.0	100.2

Comparison of average ($\bar{\sigma}$) and standard deviation (Σ_σ) in the von Mises effective stress

The total slip on the slip systems is also an interesting local metric, which will be high in regions of localized deformation. The total slip γ^T is computed locally as

$$\gamma^T = \sum_{\alpha=1}^{N_s} \int_0^{t_f} |\dot{\gamma}^\alpha| \, dt \tag{11}$$

where t_f is the time at the end of the simulation. First, we look at the distribution of slip over the polycrystal at the end of the deformation (20 % compression), where the total slip in each element is weighted by the element volume. Figure 8 compares the distributions for the middle and finest meshes for the (a) VT models and the (b) ST models. We see that the distributions are not significantly different between the two meshes. In fact, the mean and standard deviations for the middle and fine meshes are identical in each case, and the peak values are also close, changing by less than 5 % between the meshes. We also look locally at the total slip γ^T on a 2D slice cut on an ND-RD plane near the center of the grain structure, where the total slip is interpolated onto a regular 2D grid with 106 points along RD and 68 points along ND, considering only interior points. Results for the middle and finest meshes considered are shown in Fig. 9. The general pattern of the total slip is very similar between the middle and fine meshes (Fig. 9a, b for the VT model, Fig. 9c, d for the ST model), and the difference in the slip between the meshes is fairly small except near some grain boundaries (Fig. 9e, f). The median difference between meshes in total slip is 9.3 % for the VT model and 4.5 % for the ST model relative to the average slip. This indicates that a finer mesh is needed for the VT model to achieve the same level of accuracy as the ST model, which is not surprising. Some of the error between meshes is due to the interpolation onto a regular grid, especially near grain boundaries where the error is highest because the regular grid point may fall in different grains in the different meshes.

In addition to considering the difference in simulation results between the two model representations, it is also important to consider simulation costs. Because the VT models have initially uniform meshes and the element shapes are guaranteed to be optimal, the simulations with the VT model are easier to set-up, run more efficiently, and are more robust than ST models. The graph in Fig. 10 compares the efficiency between the two representations using the set of meshes described above. The simulations were run on an IBM Blue Gene L using 512 processors. From the graph, we see that the VT model is significantly more efficient for a similar number of degrees of freedom. The slow down in the simulations as the deformation progresses is due to the element distortion. Quadratic tetrahedral elements are used here for interpolating the displacement field, which, due to the mid-side nodes on the element edges, can exhibit substantial local volume change at large strains when the elements have a high aspect ratio, even though the overall volume of the elements does not change substantially. It should be noted that elastic compressibility only is allowed, while the plastic deformation, which is the majority of the deformation, is assumed incompressible. When a relatively large volume change occurs at an integration point, the integration algorithm may not converge because it is designed for large, nearly incompressible deformations, causing the step size to be cut leading to the slow down in the simulations as the deformation progresses. Ultimately, if the step size becomes too small, the simulation is ended, which is the case for the coarsest ST model that failed at about 18 % compression. Periodic remeshing may improve performance, but may also introduce error due to variable remapping and the re-equilibration process. Lower order, e.g. linear elements in displacement and constant pressure, would be more robust, but would require greater mesh refinement for accuracy. A low-order stabilized method may be a better approach, where robust and accurate P1/P1 (linear displacement and pressure) elements are used [50].

5.2 Voxel and smooth model result comparison

A number of different metrics are used to compare the results for the two geometric representations of the same grain structure. Here, we only compare the results between the VT and ST models obtained with the finest meshes considered (196,608 elements for the VT model and 194,297 elements for the ST model).

First, we compare the overall texture evolution in each case. The initial and final $\langle 111 \rangle$ equal-area pole figures are shown in Fig. 11. The pole figures are generated by weighting the orientation in each finite element by the size of the element and computing the orientation intensities in each 5° bin used to generate the pole figures. Not surprisingly, the initial pole figures are nearly identical, with small differences due to the slight difference in volumes of the initial grains
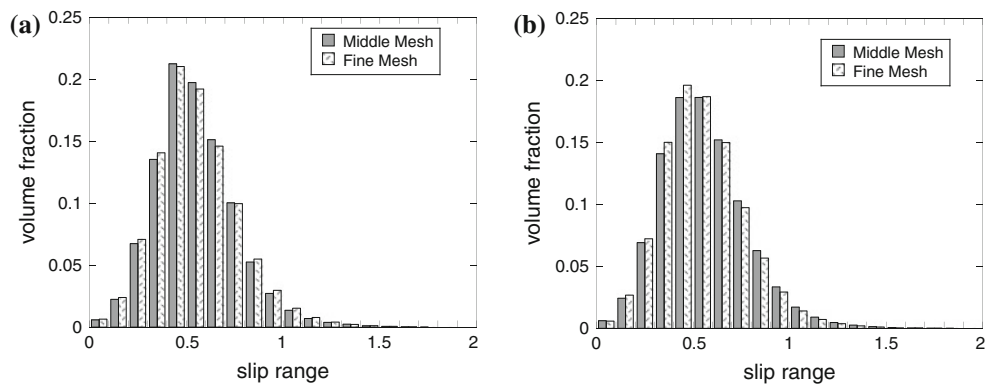
Fig. 8 Histograms showing distribution of total slip over entire polycrystal: **a** comparing the results for the VT models with 146,334 (middle mesh) and 196,608 (fine mesh) elements, and **b** comparing the results for the ST models with 146,918 (middle mesh) and 194,297 (fine mesh) elements
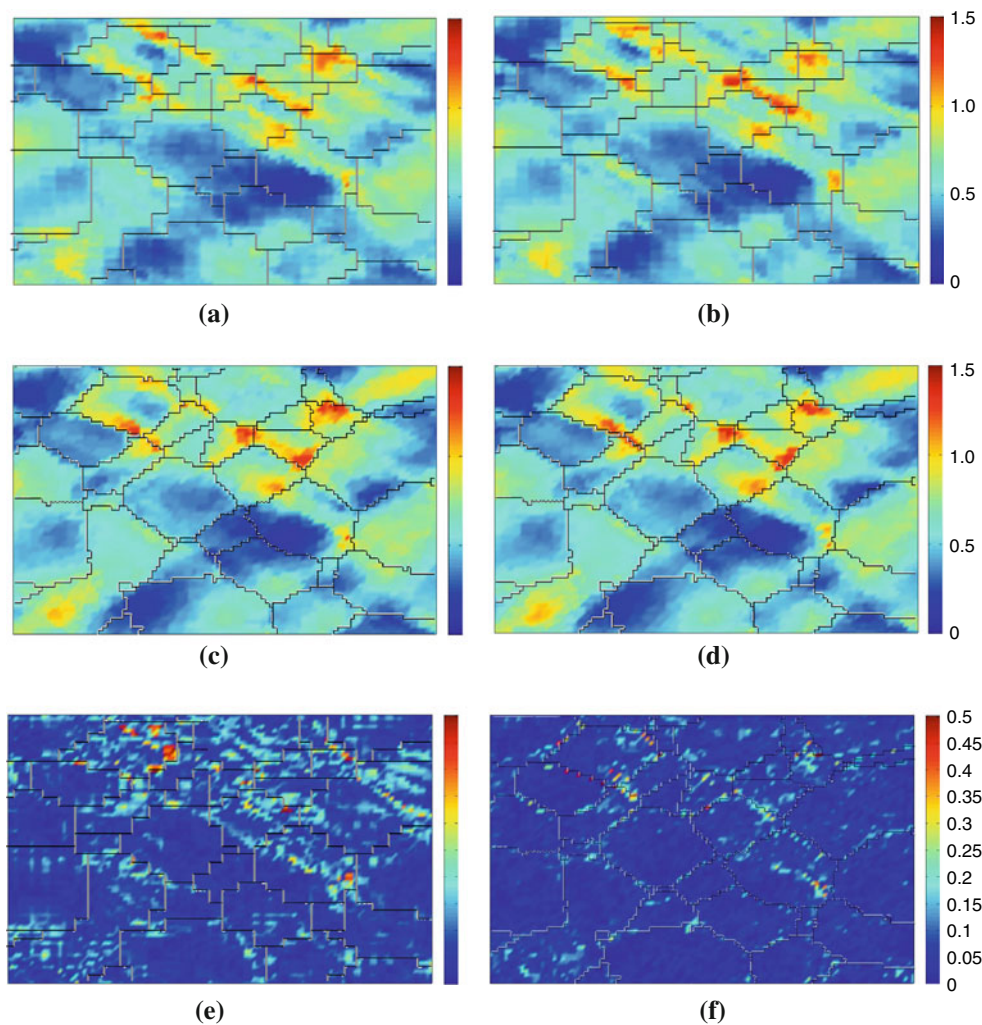

Fig. 9 Total accumulated slip interpolated onto a regular grid on a 2D slice, *horizontal* is RD, *vertical* is ND for different meshes and the difference between meshes: **a** VT model, 146,334 elements, **b** VT model, 196,608 elements, **c** ST model, 146,918 elements, **d** ST model, 194,297, **e** difference between results shown in (**a**) and (**b**) for VT models, **f** difference between results shown in (**c**) and (**d**) for ST models
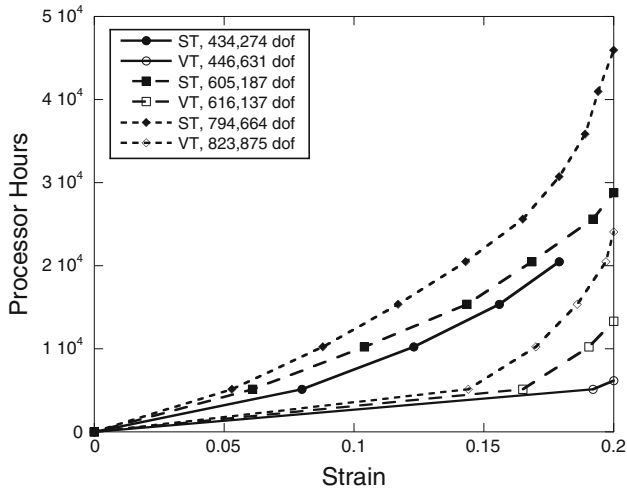
Fig. 10 Efficiency comparison for the VT (*open symbols*) and ST (*solid symbols*) representations with different mesh sizes (*dof* number of degrees of freedom)

due to the different geometric representations. Because of the small number of grains, although random orientations were assigned to the grains, there is some initial texture evident. The final pole figures are also nearly identical with the typical rolling texture starting to become apparent. The texture is slightly sharper for the VT model with the maximum texture

component intensity being 1.7 % higher in the VT model than in the ST model. Thus, the overall texture evolution does not appear to be affected by the grain structure topological representations considered here.

The macroscopic stress–strain behavior is also compared for the two models. The von Mises effective stress and strain are plotted in Fig. 12 for each model. The von Mises effective stress is computed from the Cauchy stress volume averaged over the polycrystal, and the von Mises effective strain is computed from the applied, macroscopic logarithmic strain. The macroscopic stress–strain curves for the two models are nearly indistinguishable, as can be seen in Fig. 12, with the maximum difference in stress between the curves being 8.5 MPa. Similar results are seen on a component basis too. Thus, the macroscopic stress–strain behavior is also not affected significantly by the topological representation of the grain structure for the two cases considered here. While it is not surprising that the overall texture evolution and stress–strain response are not affected by the details of the topological representation of the grain structure, one might expect that the local behavior within the grains may be affected, which is considered next.

The deformed grain structures are shown in Fig. 13. The periodicity of the deformed grain structures is evident as opposing boundaries have the same shape. We can see that
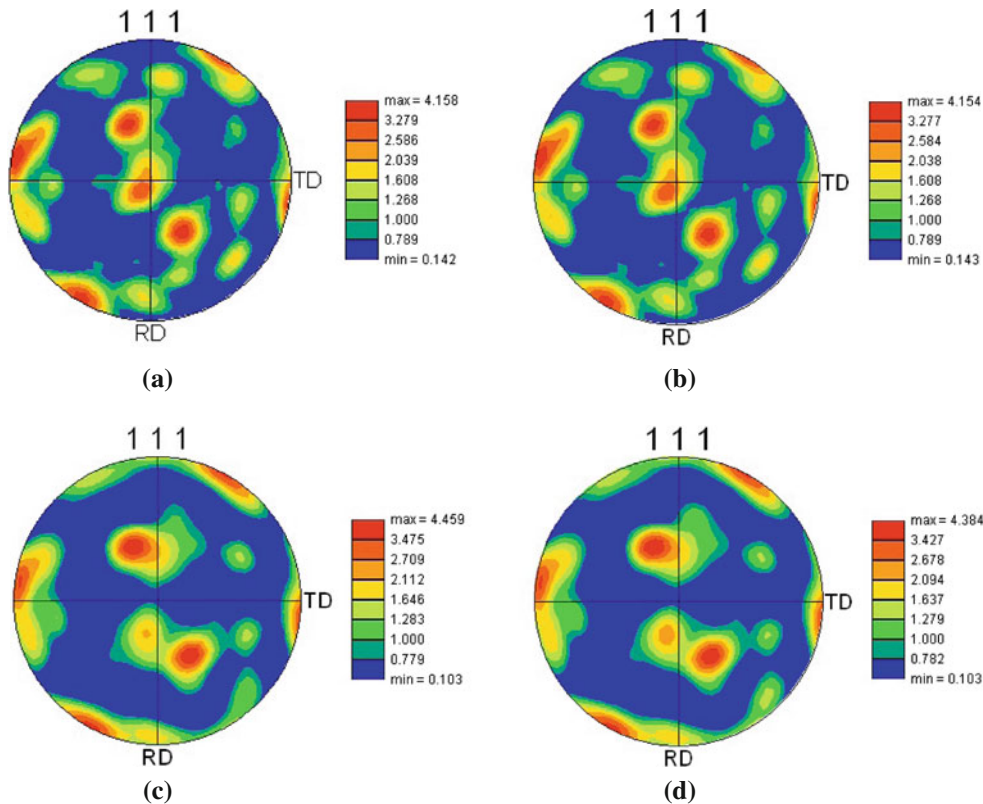

Fig. 11 Texture comparison: **a** VT initial pole figure, **b** ST initial pole figure, **c** VT final pole figure, and **d** ST final pole figure
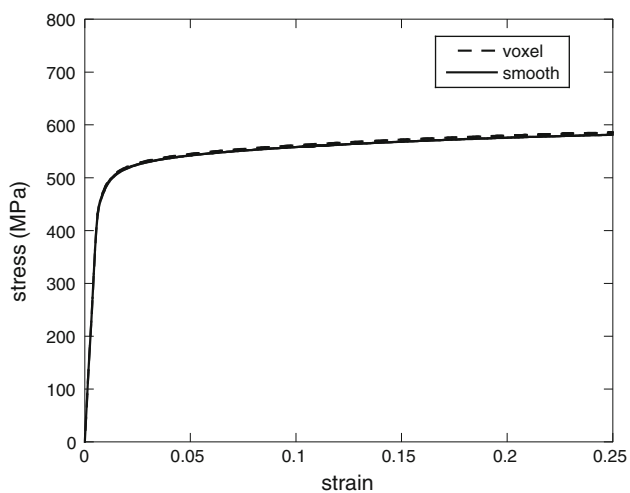
Fig. 12 The von Mises effective stress vs. strain for the two model representations

some of the grains are starting to break up with multiple orientations within the grains, shown by the color variations in the figure. The figures look quite similar as far as the overall shape of the deformed structure and the color variations appearing within the grains. The primary visible difference is the "stair-steps" on the grain boundaries in the VT model. Qualitatively, the color variations in the ST model appear to change more smoothly than in the VT model.

The primary purpose of modeling discretized grain structures is in order to capture the local fluctuation in the deformation from that of a uniform deformation. One way to quantify the non-uniformity of the deformation is to compute the average fluctuation in the displacement field from that of a uniform deformation. The average fluctuation in the displacement field between the two models is found to differ

by less than 1 % here indicating that that average level of local fluctuations in both models is not substantially different.

To examine the spatial difference in the predictions of how the grains break up in each of the models more quantitatively, we look at the intragranular misorientations that develop within the grains. First, we look at the misorientations on a 2D slice cut on an ND-RD plane, similar to the slice considered in Sect. 5.1 but at a slightly different location in the TD direction and zoomed in more to the interior of the polycrystal. The orientations are interpolated onto a regular grid on the 2D slice. The kernel average misorientation is then computed for each grid point using OIM Analysis Software [51], where the kernel average misorientation is the average misorientation between that grid point and its neighbors excluding points with misorientations greater than 10° so as not to include grain boundaries. It should be noted that we chose 10° instead of 15° here in order to better visualize the misorientations in the central parts of grains. The misorientation is strongly dependent on the grid spacing. Here, the second nearest neighbor was used in computing the misorientations in order to avoid using grid points that may lie within a single finite element.

The results are shown in Fig. 14 where the same color scale is used. Some differences in the grain structures are a direct result of the differences between the VT and ST representations. Additional differences, however, result from the influence of the stair-stepped grain boundaries on texture evolution. Note, the small stair-steps appearing in the image for the ST model result from the regular grid used by the OIM software and do not represent the actual finite element mesh used. For the ST model, the maximum misorientations appear at grain boundaries, which is not surprising as the grains may need to rotate differently near the grain boundaries from the interior in order to satisfy compatibility and equilibrium
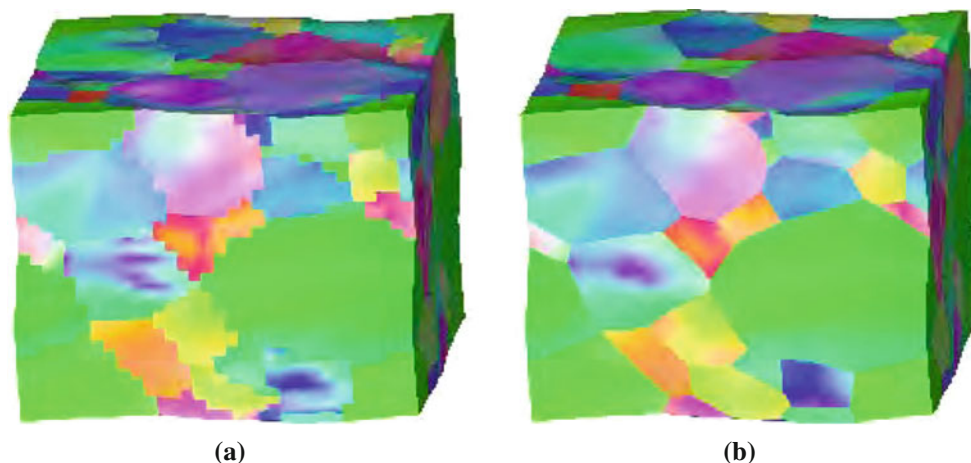

(a)   **(b)**

Fig. 13 Deformed 107 grain models used in the simulations for comparison where the grain orientations are depicted with the same ND inverse pole figure color map as in Fig. 7: **a** VT model and **b** ST model
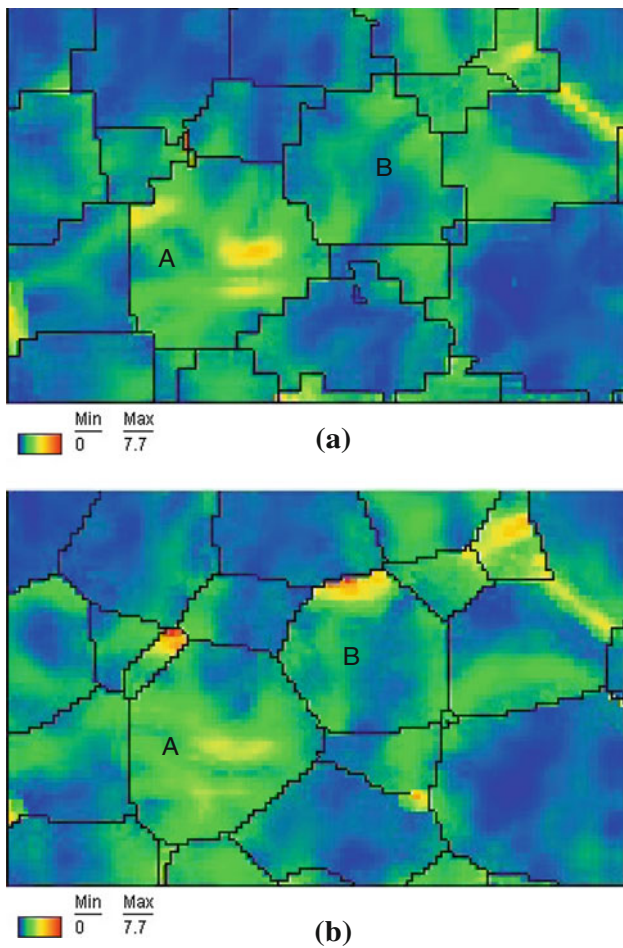
Fig. 14 Misorientation distribution on a 2D slice: **a** VT model and **b** ST model. *Horizontal* is along RD and *vertical* is along ND. Small stair-steps appearing in the ST model result from the regular grid used in the OIM imaging software and do not represent the actual finite element model used

across the grain boundary. However, in the VT model, the highest misorientations do not seem to be as concentrated near grain boundaries. This may be due to the stair-steps at

the boundary locking the boundaries resulting in stronger kinematic constraints on the grain rotations than might naturally occur. The average and maximum misorientations on the plane for the VT model are 1.11° and 6.43°, respectively, and for the ST model, they are 1.19° and 7.68°. Thus, the average and maximum misorientations predicted on the plane for the ST model are 7 and 19 % higher, respectively, than for the VT model. Looking at the individual grains labeled A and B, we can see some differences in the misorientation fields. First, looking at grain A, both models show a maximum misorientation occurring at a similar location in the grain interior, where the maximum is 3.7° in the ST model and 4.6° in the VT model. Thus, the maximum misorientation in grain A, which occurs at an interior region of the grain, is predicted to be higher in the VT model than the ST model for the given plane. On the other hand, for grain B, the ST model predicts relatively high misorientations at the upper grain boundary with a maximum of 7.5°, whereas in the VT model high misorientations are not predicted near the grain boundary and the maximum misorientation in the grain is only 2.6°.

Other local metrics that may be of interest because they may be associated with localized failure or damage are the stress state and the level of plastic deformation. Figure 15a, b show the deviatoric Cauchy stress in the ND direction (compressive) on the VT and ST deformed grain structures, respectively (refer back to Fig. 13 to see the grain structure and orientations). While the level and distribution of stress appears similar, the stress state in the ST model is much smoother than that in the VT model, where the stress distribution appears to exhibit some of the stair-stepped features at the grain boundaries. For a more quantitative analysis, a histogram of the deviatoric stress in the ND direction for the entire polycrystal is shown in Fig. 16. The distributions of the stress for both representations is very similar. Other stress components also have distributions that are similar for the ST and VT representations. It should be noted that the deviatoric stress is shown because the prescribed deformation is volume
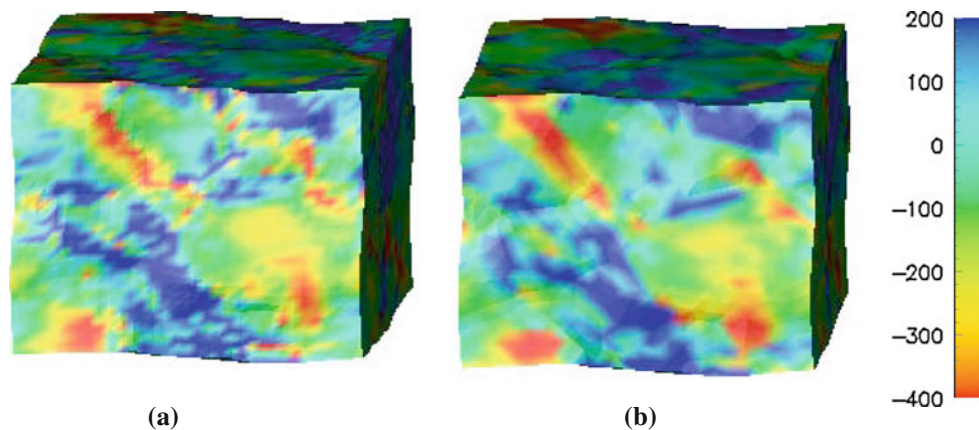

Fig. 15 Deviatoric Cauchy stress along the ND, compression direction for the **a** VT model and **b** ST model, both using the same color bar scale
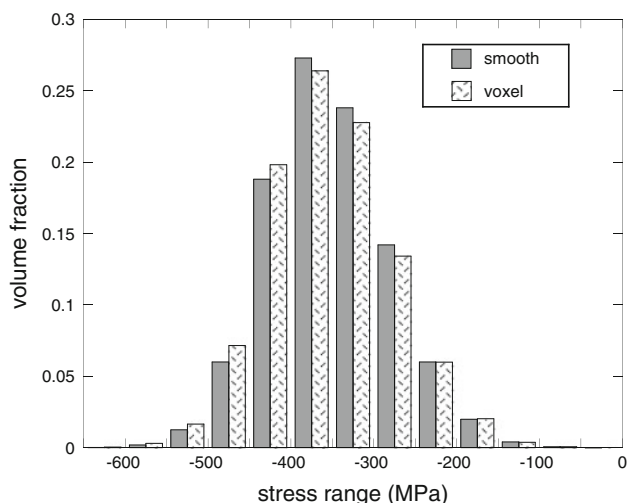
Fig. 16 Histogram showing the distribution of the deviatoric stress in the ND direction over entire polycrystal
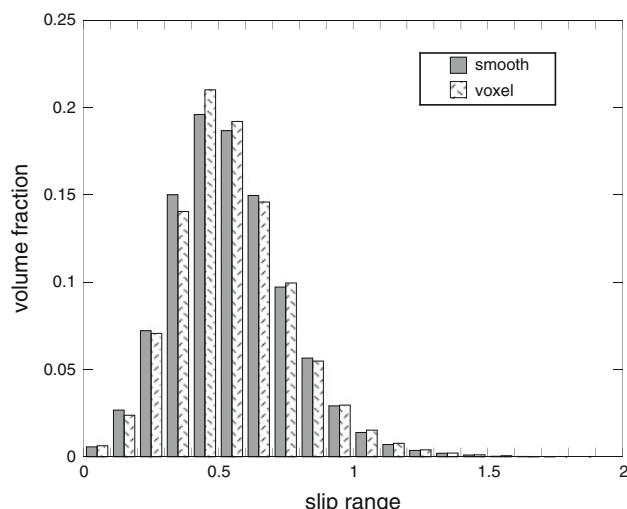

Fig. 17 Histogram showing the distribution of the total slip over entire polycrystal

Table 4 Average and standard deviation (SD) for the total (σ_{ij}) and deviatoric (σ'_{ij}) Cauchy stress components, x = RD, y = TD, z = ND, in units of MPa

	ST average	ST SD	VT average	VT SD
σ_{xx}	329	178	330	174
σ_{yy}	48	196	51	195
σ_{zz}	−339	170	−344	165
σ'_{xx}	317	92	318	94
σ'_{yy}	36	120	38	122
σ'_{zz}	−352	72	−356	74
σ_{xy}	−15	87	−15	85
σ_{xz}	29	116	29	115
σ_{yz}	7	85	7	86

preserving without any stress boundary conditions, and thus, the computation of the hydrostatic stress will be less reliable for the nearly incompressible behavior. However, since a stable, mixed finite element formulation is used, the full stress components have a similar smoothness and exhibit similar trends. The average and standard deviations for all the deviatoric and total stress components are given in Table 4.

Finally, the total slip, computed as described in Sect. 5.1 (Eq. 11), is compared. The distribution of total slip for each model representation is compared in Fig. 17. The distributions for the ST and VT models are very similar. The average total slip for the ST model is 0.54 and for the VT, it is 0.55, and the standard deviation in the total slip for both models is 0.21. Thus, key statistical metrics in the stress and total slip are very close for both representations. If we look again at the total slip on the 2D slices shown in Fig. 9b, d), we see a similar pattern with regions of high localized slip occurring

mostly at grain boundaries, but also some regions within the interior of grains. The mean difference in slip on the 2D slices between the VT and ST models is 14.9 % and the median difference is 10.5 %.

6 Conclusions

Two geometric representations of a polycrystal grain structure, one with the grains represented as a collection of voxels (VT) resulting in stair-stepped grain boundaries, and one with smooth grain boundaries (ST), are modeled and the predicted fields and efficiencies are compared. Both models gave very similar results with regard to the following:

– overall texture evolution,
– macroscopic stress–strain behavior,
– average level of local fluctuation in the displacement field,
– statistical distribution of stress, and
– statistical distribution of total slip on the slip systems.

The most significant difference in the simulation results appeared in the misorientation distributions. The ST model predicted higher misorientations near grain boundaries that were not observed in the VT model, and a higher maximum misorientation on a typical plane was predicted by the ST model. It was also observed that the stress field within the grains is smoother in the ST model than in the VT model, where the stress distribution exhibited some of the stair-stepped features of the grain boundaries. The local distribution of slip was also found to exhibit some difference between the models. The VT model was more robust and efficient because the initial finite element mesh consisted of uniform

elements, and thus had a better mesh quality with the elements less likely to exhibit problems under severe distortion, especially here where quadratic, tetrahedral elements were used. Lower order elements would be more robust at large strains.

Based on these results, if an accurate misorientation distribution is important to the analyst, for example to predict the breaking up of the grains into sub-grains and the formation of low angle boundaries, the ST model should be used. Otherwise, a VT model may provide adequate accuracy with better efficiency and ease of model creation. Efficiency in the ST model could be improved, and may surpass the VT model, if graded meshes were used, for example with initially finer meshing near grain boundaries and coarser meshing on the grain interiors, and if lower order elements in a stabilized finite element framework were used. Finally, this study did not specifically investigate the number of voxels per grain required to model a polycrystal with the same accuracy as an ST model, which would be interesting for a future study.

References

1. Taylor GI (1938) Plastic strains in metals. J Inst Metals 62(1): 307–324
2. Asaro RJ, Needleman A (1985) Texture development and strain hardening rate dependent polycrystals. Acta Metall 33:923–953
3. Mathur KK, Dawson PR (1989) On modeling the development of crystallographic texture in bulk forming processes. Int J Plast 5: 67–94
4. Canova GR, Kocks UF, Jonas JJ (1984) Theory of torsion texture development. Acta Metall 32:211–226
5. Mathur KK, Dawson PR, Kocks UF (1990) On modeling anisotropy in deformation processes involving textured polycrystals with distorted grain shape. Mech Mater 10:183–202
6. Molinari A, Canova GR, Ahzi A (1987) A self consistent approach of the large deformation polycrystal viscoplasticity. Acta Metall 35:2983–2994
7. Fleck N, Muller G, Ashby M, Hutchinson J (1994) Strain gradient plasticity: Theory and experiment. Acta Metall Mater 42:475–487
8. Beaudoin AJ, Acharya A, Chen SR, Korzekwa DA, Stout MG (2000) Consideration of grain-size effect and kinetics in the plastic deformation of metal polycrystals. Acta Mater 48:3409–3423
9. Janssen PJM, Hoefnagels JPM, de Keijsera TH, Geers MGD (2008) Processing induced size effects in plastic yielding upon miniaturisation. J Mech Phys Solids 56:2687–2706
10. Beaudoin AJ, Mecking H, Kocks UF (1996) Development of localized orientation gradients in fcc polycrystals. Philos Mag A 73:1503–1517
11. Sarma GB, Radhakrishnan B, Zacharia T (1998) Finite element simulations of cold deformation at the mesoscale. Comput Mater Sci 12:105–122
12. Hochhalter JD, Littlewood DJ, Christ Jr RJ, Veilleux MG, Bozek JE, Ingraffea AR, Maniatty AM (2010) A geometric approach to modeling microstructurally small fatigue crack formation: II. Physically based modeling of microstructure-dependent slip localization and actuation of the crack nucleation mechanism in AA 7075-T651. Modell Simul Mater Sci Eng 18:045004
13. Roters F, Eisenlohr P, Hantcherli L, Tjahjanto D, Bieler T, Raabe D (2010) Overview of constitutive laws, kinematics, homogenization and multiscale methods in crystal plasticity finite-element modeling: Theory, experiments, applications. Acta Mater 58:11521211
14. Van Houtte P, Delannay L, Kalidindi SR (2002) Comparison of two grain interaction models for polycrystal plasticity and deformation texture prediction. Int J Plast 18:359–377
15. Anand L (2004) Single-crystal elasto-viscoplasticity: application to texture evolution in polycrystalline metals at large strains. Comput Methods Appl Mech Eng 193:5359–5383
16. Li S, Kalidindi SR, Beyerlein IJ (2005) A crystal plasticity finite element analysis of texture evolution in equal channel angular extrusion. Mater Sci Eng A 410(411):207–212
17. Buchheit TE, Wellman GW, Battaile CC (2005) Investigating the limits of polycrystal plasticity modeling. Int J Plast 21(2):221–249
18. Fülöp T, Brekelmans WAM, Geers MGD (2006) Size effects from grain statistics in ultra-thin metal sheets. J Mater Process Technol 174:233–238
19. Nakamachi E, Hiraiwa K, Morimoto H, Harimoto M (2000) Elastic/crystalline viscoplastic finite element analyses of single- and poly-crystal sheet deformations and their experimental verification. Int J Plast 16:1419–1441
20. Ritz H, Dawson PR (2009) Sensitivity to grain discretization of the simulated crystal stress distributions in fcc polycrystals. Model Simul Mater Sci Eng 17:015001
21. Kanit T, Forest S, Galliet I, Mounoury V, Jeulin D (2003) Determination of the size of the representative volume element for random composites: Statistical and numerical approach. Int J Solids Struct 40:3647–3679
22. Zhang KS, Wu MS, Feng R (2005) Simulation of microplasticity-induced deformation in uniaxially strained ceramics by 3-d voronoi polycrystal modeling. Int J Plast 21:801–845
23. Zeghadi A, N'guyen F, Forest S, Gourgues AF, Bouaziz O (2007) Ensemble averaging stress–strain fields in polycrystalline aggregates with a constrained surface microstructure—part 1: anisotropic elastic behaviour. Philos Mag 87:1401–1424
24. Zeghadi A, Forest S, Gourgues AF, Bouaziz O (2007) Ensemble averaging stress–strain fields in polycrystalline aggregates with a constrained surface microstructure—part 2: crystal plasticity. Philos Mag 87:1425–1446
25. Anderson MP, Grest GS, Srolovitz DJ (1989) Computer simulation of normal grain growth in three dimensions. Philos Mag B 59:293–329
26. Radhakrishnan B, Zacharia T (1995) Simulation of curvature-driven grain growth by using a modified Monte Carlo algorithm. Metall Mater Trans A 26:167–180
27. Moelans N, Blanpain B, Wollants P (2005) A phase field model for the simulation of grain growth in materials containing finely dispersed incoherent second-phase particles. Acta Mater 53:1771–1781
28. Marx V, Reher F, Gottstein G (1999) Simulation of primary recrystallization using a modified three-dimensional cellular automaton. Acta Mater 47:1219–1230

29. Saylor DM, Fridy J, El-dasher BS, Jung KY, Rollett AD (2004) Statistically representative three-dimensional microstructures based on orthogonal observation sections. Metall and Mater Trans A 35:1969–1979

30. St-Pierre L, Heripre E, Dexet M, Crepin J, Bertolino G, Bilger N (2008) 3d simulations of microstructure and comparison with experimental microstructure coming from OIM analysis. Int J Plast 24:1515–1532

31. Claves SR, Bandar AR, Misiolek WZ, Michael JR (2004) Three-dimensional (3d) reconstruction of AlFeSi intermetallic particles in 6xxx aluminum alloys using the focused ion beam. Microsc Microanal 10:1138–1139

32. Poulsen SO, Lauridsen EM, Lyckegaard A, Oddershede J, Gundlach C, Curfs C, Jensen DJ (2011) In situ measurements of growth rates and grain-averaged activation energies of individual grains during recrystallization of 50 % cold-rolled aluminium. Sci Mater 64:1003–1006

33. Lorensen WE, Harvey EC (1987) Marching cubes: a high resolution 3d surface construction algorithm. In: Computer graphics. SIGGRAPH 87 conference proceedings. ACM, New York, pp 163–169

34. Amenta N, Bern M, Kamvysselis M (1998) A new Voronoi-based surface reconstruction algorithm. In: Computer graphics. SIGGRAPH 98 conference proceedings. ACM, New York, pp 415–421

35. Chernyaev EV (1995) Marching cubes 33: construction of topologically correct isosurfaces. Technical report CN/95-17. CERN, Geneva

36. Carneiro BP, Silva CT, Arie EK (1996) Tetra-cubes: an algorithm to generate 3d isosurfaces based upon tetrahedra. In: Anais do IX SIBGRAPI'96, Sociedade Brasileira de Computacao, pp 205–210. SBC, Brasil

37. Tarini M, M Callieri CM, Rocchini C (2002) Marching intersections: an efficient approach to shape-from-silhouette. In: 7th International fall workshop of vision, modeling, and visualization, vol 603. DFG Graduate Research Center SFB, Erlangen, pp 255–262

38. Wiederkehr T, Klusemann B, Gies D, Mller H, Svendsen B (2010) An image morphing method for 3d reconstruction and FE-analysis of pore networks in thermal spray coatings. Comput Mater Sci 47:881–889

39. Lewiner T, Lopes H, Vieira AW, Tavares G (2003) Efficient implementation of marching cubes' cases with topological guarantees. J Graph Tools 8:1–15

40. Cahn JW, Van Vleck ES (1999) On the co-existence and stability of trijunctions and quadrijunctions in a simple model. Acta Metall 47:4627–4639

41. Abaqus (2009) Analysis user's manual, version 6.9. Dassault Systemes Simulia Corporation, Providence

42. Bozek JE, Hochhalter JD, Veilleux MG, Liu M, Heber G, Sintay SD, Rollett AD, Littlewood DJ, Maniatty AM, Weiland H, Christ Jr RJ, Payne J, Welsh G, Harlow DG, Wawrzynek PA, Ingraffea AR (2008) A geometric approach to modeling microstructurally small fatigue crack formation: I probabilistic simulation of constituent particle cracking in AA 7075 T651. Model Simul Mater Sci Eng 16:065007

43. Gurtin ME (2003) An introduction to continuum mechanics. Academic Press, San Diego

44. Lee EH (1969) Elastic–plastic deformation at finite strain. J Appl Mech 36:1–6

45. Maniatty AM, Dawson PR, Lee YS (1992) A time integration algorithm for elasto-viscoplastic cubic crystals applied to modeling polycrystalline deformation. Int J Numer Methods Eng 35:1565–1588

46. Matouš K, Maniatty AM (2004) Finite element formulation for modeling large deformations in elasto-viscoplastic polycrystals. Int J Numer Methods Eng 60:2312–2333

47. Matouš K, Maniatty AM (2009) Multiscale modeling of elasto-viscoplastic polycrystals subjected to finite deformations. Interact Multisc Mechs 2:375–396

48. Pyle D (2009) A comparison of 2 methods for FEM simulations of discretized polycrystals. M.S. Thesis. Rensselaer Polytechnic Institute, Troy

49. Argonne National Laboratory (2011). http://www.mcs.anl.gov/petsc/. Accessed 12 Jan 2011

50. Ramesh B, Maniatty AM (2005) Stabilized finite element formulation for elasticplastic finite deformations. Comput Methods Appl Mech Eng 194:775–800

51. EDAX (2010) OIM Analysis Software, Materials Analysis Division. Ametek Inc., Mahwah